Nanoscale

ROYAL SOCIETY OF CHEMISTRY

PAPER

View Article Online
View Journal | View Issue

Cite this: *Nanoscale*, 2023, **15**, 5834

Electrosynthesis of Au nanocluster embedded conductive polymer films at soft interfaces using dithiafulvenyl-functionalized pyrene†

Reza Moshrefi, Katelyn Ryan, Evan P. Connors, Joshua C. Walsh, Erika Merschrod, Graham J. Bodwell and Talia Jane Stockmann *

Nanoparticle (NP) embedded conductive polymer films are desirable platforms for electrocatalysis as well as biomedical and analytical applications. Increased catalytic and analytical performance is accompanied by concomitant decreases in NP size. Herein, highly reproducible electrogeneration of low dispersity Au nanocluster embedded ultra-thin (~2 nm) conductive polymer films at a micro liquid|liquid interface is demonstrated. Confinement at a micropipette tip facilitates a heterogeneous electron transfer process across the interface between two immiscible electrolyte solutions (ITIES), between $KAuCl_4$(aq) and a dithiafulvenyl-substituted pyrene monomer, 4,5-didecoxy-1,8-bis(dithiafulven-6-yl)pyrene (bis(DTF) pyrene), in oil, *i.e.*, a w|o interface. At a large ITIES the reaction is spontaneous, rapid, and proceeds *via* transfer of $AuCl_4^-$ to the oil phase, followed by homogeneous electron transfer generating uncontrolled polymer growth with larger (~50 nm) Au nanoparticles (NPs). Thus, miniaturization facilitates external, potential control and limits the reaction pathway. Atomic (AFM) and Kelvin probe force microscopies (KPFM) imaged the topography and work function distribution of the as-prepared films. The latter was linked to nanocluster distribution.

Received 21st November 2022,
Accepted 27th February 2023

DOI: 10.1039/d2nr06519c

rsc.li/nanoscale

Introduction

The ITIES, *i.e.*, the liquid|liquid or soft interface, has come under increasing interest as a platform for the growth/synthesis of 2D and 3D molecular[1,2] and nano-structures,[3–7] as well as for electrosynthesis of electrocatalytic materials and conductive polymers.[8,9] The Galvani potential difference, *e.g.*, between water|oil (w|o), $\phi_w - \phi_o = \Delta_o^w\phi$, is localized across the interface and controlled with electrodes immersed in either phase positioned relatively far away; thus, this approach is often referred to as 'electrodeless' since electrodes are only indirectly involved. Since the electrodes are not physically or chemically engaged in the electrosynthetic process, one can exploit the pristine, molecularly smooth, defect-free features of the liquid|liquid interface, that lends itself to a high degree of experimental reproducibility. This is advantageous since solid/solution interfaces often carry the risk that morphological features from the solid substrate will be transcribed onto the synthesized material which can inhibit their ultimate functionality; moreover, the material is often covalently bound to the solid surface complicating its removal and application as a free-standing material. These materials, whether nanoparticle[3,5–7,10] or molecular assemblies[1,2] as well as polymer films,[8,9] have potential use in biomedical, electrocatalytic, and separation science applications.

Early work in externally controlled electropolymerization reactions at liquid|liquid interfaces was performed by Cunnane's group and focused on monomers/electron donors such as 2,2′:5′,2″-terthiophene (TT),[11–14] and functionalized pyrroles.[15] Meanwhile, Mareček's group tested three different modified pyrroles.[16] Similarly, Dryfe's group electrogenerated polypyrrole in the presence of single-walled carbon nanotubes (SWCNTs), which were physically deposited at the liquid|liquid interface, generating a SWCNT/polymer composite material. During this time, electrogeneration of metal nanoparticles (NPs) at soft interfaces was also being explored by Johans *et al.*,[17–20] while Knake *et al.*[21] demonstrated the feasibility of simultaneous Au NP generation and tyramine polymerization at a large ITIES electrosynthesizing a nanocomposite material.

More recently, however, Lehane *et al.*[8] demonstrated the electrosynthesis of poly(3,4-dioxyethylene)thiophene (PEDOT) at a macro liquid|liquid interface (cm scale) between water|α,α,α-trifluorotoluene (w|TFT), using Ce^{4+} as an electron acceptor in the aqueous phase with EDOT dissolved in TFT. They were able to reproducibly electrogenerate films <50 nm thick that could be extracted from the interface, stored for

Memorial University of Newfoundland, Core Science Facility, 45 Arctic Ave, St. John's, NL, Canada, A1C 5S7. E-mail: tstockmann@mun.ca

† Electronic supplementary information (ESI) available. See DOI: https://doi.org/10.1039/d2nr06519c

long-term use, and were shown to be biocompatible. Then, our group demonstrated further synthetic control through miniaturization of the ITIES and building on the works for Cunnane and others with simultaneous Au[9] and Cu[22] NP generation and TT electropolymerization. This approach relied on performing the electrosynthesis at a micro-ITIES (25 μm in diameter), while installing the metal salt (*e.g.*, $KAuCl_4$) in the aqueous phase and TT in 1,2-dichloroethane (DCE). In this way, the large overpotentials thought necessary by Cunnane could be avoided,[14] limiting overoxidation of the film.[23]

Herein, a pyrene skeleton has been functionalized with two dithiafulvenyl (DTF) substituents to create a highly electron-donating molecule, 4,5-didecoxy-1,8-bis(dithiafulven-6-yl) pyrene (**1**, Fig. 1). Pyrene has become ubiquitous in synthetic, macromolecular, and supramolecular chemistry as a framework on which one can build a wide variety of materials.[24–26] This is enhanced further due to its ready availability industrially as well as owing to its electronic properties. The latter, combined with it being a chromophore have led to pyrenes being active components in organic light emitting diodes (OLEDs) and other organic electronic devices.[26] Similarly, the DTF dimerization mechanism through the formation of a radical cation species is well known and has been employed in the preparation of π-conjugated conductive polymers[27,28] as well as metal NPs.[29] Khadem *et al.*[30] showed that a molecule similar to the bis(DTF)pyrene **1** (see Fig. 1) was extremely resistant to oxidative coupling despite having two relatively low oxidation potentials at 0.57 and 0.72 V (*vs.* Ag/AgCl) which were attributed to the successive oxidation of the two DTF moieties.

Nevertheless, low dispersity Au nanoclusters (~1.7 nm in diameter) embedded in polymer films were electrosynthesized at a polarizable micro w|DCE interface (25 μm in diameter) through application of **1** as an electron donor dissolved in the DCE phase and $KAuCl_4$ in aqueous. The voltammetric evolution of an electron transfer wave with a concomitant decrease in the signal for $AuCl_4^-$ simple ion transfer with increasing concentration of **1**, c_m, was observed. Films were then ejected from the tip of the micropipette using a syringe attached to the back of the specialized holder and deposited on Au and glass substrates. Atomic force microscopy (AFM) and Kelvin probe force microscopy (KPFM) were used to image the topography of the nanocomposite film and estimate the film thickness, as well as the change in work function across the material, which is linked to the distribution of Au nanoclusters.

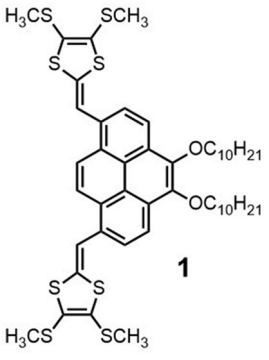

Fig. 1 Chemical structure of 4,5-didecoxy-1,8-bis(dithiafulven-6-yl) pyrene (**1**).

Experimental

All chemicals were used as received without purification. Potassium tetrachloroaurate ($KAuCl_4$, >98%), hydrochloric acid solution (HCl, >37%), 1,2-dichloroethane (DCE, >98%), trioctylphosphine (97%), trihexyltetradecylphosphonium bromide ($P_{66614}Br$, >95%), and bromooctane (99%) were purchased from Sigma-Aldrich/Merck. Lithium tetrakis(pentafluorophenyl)borate etherate (LiTB, ≥99%) was sourced from Boulder Scientific. The organic phase supporting electrolyte tetraoctylphosphonium tetrakis(pentafluorophenyl)borate ($P_{8888}TB$) and $P_{66614}TB$ (trihexyltetradecylphosphonium tetrakis(pentafluorophenyl)borate) were prepared as described elsewhere.[7,31] Similarly, the preparation of bis(DTF)pyrene **1** has also been reported.[30]

A PG-618-USB potentiostat (Heka Electroniks) was employed to record all electrochemical measurements. The aqueous phase was injected into a micropipette held inside a specialized holder. The holder was equipped with an integrated Au wire which was immersed in the aqueous phase and connected externally using an SMA connector to the head-stage of the potentiostat serving as the working electrode. The counter/reference electrode was a Pt wire also connected to the head-stage and immersed in the organic phase. The interface between two immiscible electrolyte solutions (ITIES) with a diameter of 25 μm was maintained at the micropipette tip and monitored by a CCD camera (AmScope) attached to a magnifying lens assembly (Navitar). Micropipettes composed of borosilicate glass (Goodfellow Inc.) and modified holder have been described in detail in earlier reports as well as briefly in the ESI.†[32] The electrolytic cells employed throughout have been drawn in Scheme 1 and all experiments were performed in a 2-electrode configuration unless indicated otherwise.

The experimental potential scale was referenced to the Galvani scale using the simple Cl^- transfer, using the formal Cl^- transfer potential ($\Delta_o^w\phi^{o'}_{Cl^-}$), −0.479 V, described by Zhou *et al.*[33]

A Tecnai Spirit Transmission Electron Microscope (TEM) was employed to image nanocomposite samples deposited on 2 μm holey Au and 200 mesh Cu TEM grids (Electron Microscopy Sciences). After samples were deposited onto a TEM grid, they were dried under a flow of N_2 gas.

The topography and work function maps were taken using the MFP-3D (AFM/KPFM) from Asylum research equipped with NSC/Pt or NSC35/AL BS tips (MikroMasch) operating at a scan rate of 0.25 Hz for KPFM or AFM topography/scratch test, respectively. The platinum tips' work function was determined using HOPG as a standard.

$$\mathrm{Au}\left|\mathrm{AuCl_3}\right|\begin{matrix}10\ \mathrm{mM\ HCl}\\ x\ \mathrm{mM\ KAuCl_4}\\ (aq)\end{matrix}\Big\|\begin{matrix}y\ \mathrm{mM}\ \mathbf{1}\\ 5\ \mathrm{mM\ P_{8888}TB}\\ (DCE)\end{matrix}\Big|\mathrm{PtTB}\Big|\mathrm{Pt}\qquad[\text{Cell 1}]$$

$$\mathrm{Au}\left|\mathrm{AuCl_3}\right|\begin{matrix}x\ \mathrm{mM\ KAuCl_4}\\ (aq)\end{matrix}\Big\|\begin{matrix}y\ \mathrm{mM}\ \mathbf{1}\\ 5\ \mathrm{mM\ P_{8888}TB}\\ (DCE)\end{matrix}\Big|\mathrm{PtTB}\Big|\mathrm{Pt}\qquad[\text{Cell 2}]$$

$$\mathrm{Au}\left|\mathrm{AuCl_3}\right|\begin{matrix}5\ \mathrm{mM\ KCl}\\ (aq)\end{matrix}\Big\|\begin{matrix}y\ \mathrm{mM}\ \mathbf{1}\\ 5\ \mathrm{mM\ P_{8888}TB}\\ (DCE)\end{matrix}\Big|\mathrm{PtTB}\Big|\mathrm{Pt}\qquad[\text{Cell 3}]$$

Scheme 1 Electrolytic cells where *y* mM of **1** as the electron donor (see Fig. 1) was added to the organic phase. Meanwhile, *x* mM of $KAuCl_4$ (aq) was added to the aqueous phase in Cells 1 and 2. Tetraoctylphosphonium tetrakis(pentafluorophenyl)borate ($P_{8888}TB$) ionic liquid was employed as the organic phase supporting electrolyte. The double-bars indicate the 25 μm diameter polarizable liquid|liquid interface.

Results and discussion

Cyclic voltammograms (CVs) shown in Fig. 2 were recorded using Cells 1, 2, and 3 for the red, black, and blue, dashed traces, respectively, with y = 0 mM in the DCE phase, *i.e.*, no bis(DTF)pyrene **1** added, while 5 mM of $KAuCl_4$ was added to the aqueous phase for Cells 1 and 2. In each case, the limit of the polarizable potential window (PPW) is described by the large increase in the magnitude of the current at roughly 0.5 and −0.5 V; whereby, the respective K^+/H^+ and Cl^- supporting electrolyte ions undergo simple ion transfer from water to oil (w → o) and back.[4] The organic phase supporting electrolyte ions, P_{8888}^+ and TB^-, are minor contributors to the PPW limiting signal.[34] The blue, dashed curve depicts the response without $KAuCl_4$ added to the aqueous phase and represents a blank trace. At pH ~5.5 using Cell 2 with 5 mM of $KAuCl_4$(aq) (black curve in Fig. 2), the peak-shaped waves at 0.126 V and −0.013 V when scanning from positive to negative potentials are due to the simple ion transfer of $AuCl_4^-$ and $AuCl_{(4-\gamma)}(OH)_\gamma^-$ from w → o, respectively. It is recognized that $AuCl_4^-$ undergoes ligand speciation at moderate to high pH forming $AuCl_{(4-\gamma)}(OH)_\gamma^-$ in which γ chlorides have been replaced by hydroxide ligands; thus, these data are in good agreement with recent reports.[9,10,35–37] The two steady-state waves with half-wave potentials ($\Delta_o^w\phi_{1/2}$) at roughly −0.009 and 0.177 V present during the reverse scan using Cell 2 correspond to the respective transfers of $AuCl_{(4-\gamma)}(OH)_\gamma^-$ and $AuCl_4^-$ back from o → w. At pH 2 in the aqueous phase (red curve in Fig. 2), only one signal corresponding to $AuCl_4^-$ transfer was observed. The asymmetric *i*–*V* response between the forward and reverse scan directions is owing to geometric confinement within the micropipette leading to linear and hemispherical diffusion inside and outside of the pipette, respectively; this agrees well with previous studies.[7,38]

Fig. 3 shows the *i*–*V* responses for Cells 1 and 2 with increasing concentrations of **1** (c_m) in DCE and $KAuCl_4$ in the aqueous phase. Only a small amount of **1** added to the DCE phase changes the voltammetric response resulting in a positive peak-shaped wave at potentials greater than the ion transfer potential for $AuCl_4^-$. For example, in Fig. 3C using Cell 1 with [$KAuCl_4$] = 5 mM, and with increasing c_m, there is a concomitant decrease in the peak intensity for $AuCl_4^-$ ion transfer signal from w → o and the development of a new signal at

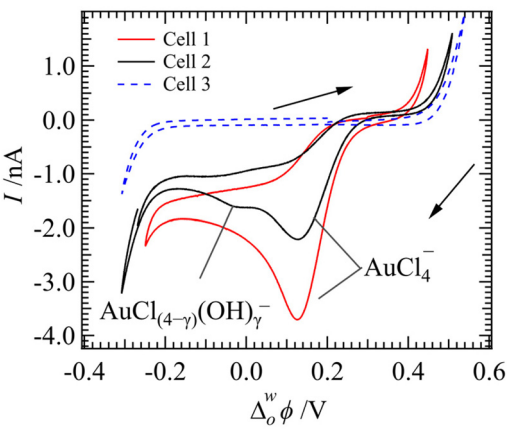

Fig. 2 Cyclic voltammograms (CVs) recorded using Cells 1, 2, and 3 as indicated inset at 0.020 V s^{-1} with **1** = 0 mM in DCE and 5 mM $KAuCl_4$ (aq) in Cells 1 and 2. Solid black arrows indicate scan direction. Each peak-shaped wave is labeled with the ion undergoing transfer across the ITIES from w → o.

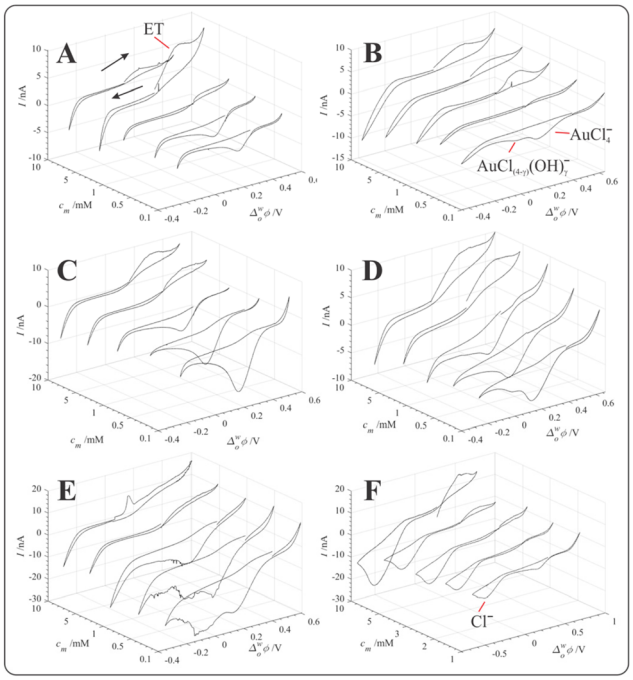

Fig. 3 Overlay of CVs obtained at a 25 μm diameter micro-ITIES using Cells 1 and 2 for the left (**A**, **C**, **E**) and right-hand columns (**B**, **D**, **F**), with [$KAuCl_4$] or x = 1, 5, and 10 mM for the top, middle, and bottom panels, respectively. While c_m was the concentration of **1** (see Fig. 1) added to the DCE phase. Arrows indicate scan direction, and the CV was swept at a rate of 0.020 V s^{-1}. ET = electron transfer wave; the simple ion transfer signals have been labelled with their associated ions inset.

~0.35 V. At modest c_m with a [$KAuCl_4$] : [bis(DTF)pyrene] ratio of less than 1 : 1, but greater than 1 : 0.5, the *i–V* signal is sigmoidal; however, a ratio of 1 : 2 results in a peak-shaped wave. The DTF and pyrene core of **1** are both good electron donors; therefore, it is proposed that this is interfacial electron transfer from **1** in oil to $AuCl_4^-$/$AuCl_{(4-\gamma)}(OH)_\gamma^-$ in water, *i.e.*, a negative charge being transferred from o → w. This agrees well with the transition from sigmoidal to peak-shaped wave, since at low c_m electron transfer would be diffusion limited by **1** in the organic phase; whereby, the electron donor is operating under a hemispherical diffusion regime.[38] Compound **1** is presumably very hydrophobic so unlikely to partition into the aqueous phase. Owing to the high redox potential of $AuCl_4^-$, $E^{o'}_{AuCl_4^-/Au} = 1.002$ V,[39] the Au salt is likely reduced to Au^0 generating metal nanoparticles (NPs). This agrees well with our recent reports using ferrocene (Fc)[7] and TT[9,22] as organic phase electron donors, as well as Bai *et al.*'s electrosynthesis of Ag wire at a nanopipette interface.[40]

The oxidation potential of **1** was determined by dissolving ~1 mM of the monomer in DCE and recording the CV at a Pt inlaid disc ultramicroelectrode (UME), with a radius of 12.5 μm, and with the potential referenced to the ferrocene redox couple (Fc^+/Fc) as described previously,[41] with $E^{o'}_{Fc^+/Fc} = 0.64$ V (*vs.* SHE).[42] Thus, $E^{o'}_{1^+/1}$ was determined to be ~1.6 V (*vs.* SHE). The heterogeneous electron transfer mechanism can be described generally by the following two equations for the system at pH 2 and 5.5–6, respectively,

$$AuCl_4^-(aq) + 3D(org) \rightarrow Au(s) + 3D^{+\bullet}(org) + 4Cl^-(aq) \quad (1)$$

$$AuCl_{(4-\gamma)}(OH)_\gamma^-(aq) + \gamma H^+(aq) + 3D(org) \rightarrow Au(s) + 3D^{+\bullet}(org) + (4-\gamma)Cl^-(aq) + \gamma H_2O(l) \quad (2)$$

in which, *D* is the electron donor, **1**. Using established analytical solutions[4,42] the approximate electron transfer potential ($\Delta^w_o\phi_{ET}$) can be formulated as,

$$\Delta^w_o\phi_{ET} \approx E^{o',DCE}_{1^+/1} - E^{o',H_2O}_{Au(III)/Au} - \frac{(0.059\,V)}{3}\log([H^+]^\gamma) \quad (3)$$

Since there is no $AuCl_4^-$ speciation at pH 2, the logarithmic term on the right-hand side is ignored in that case. Thus, $\Delta^w_o\phi_{ET}$ was calculated to be 0.67 and 0.56 V at pH 2 and 5.5–6, respectively, meaning a lower applied potential is needed at moderate pH, which agrees with the voltammetric results and the improved film formation (see below) using Cell 2.

To investigate the formation of NPs, aqueous droplets were ejected out of the micropipette after performing 25 consecutive CV cycles, deposited onto a 2 μm holey Au TEM grid, dried with N_2 gas, and imaged (Fig. 4). Fig. 4A shows the Au NP/poly-bis(DTF)pyrene composite obtained at pH ~5.5 with [$KAuCl_4$] and c_m equal to 5 and 1 mM, respectively. In this case, the film completely occludes the 2 μm hole in the TEM grid. At pH 2 under otherwise similar conditions, the film was poorly formed (Fig. 4B). Fig. 4C shows a magnified section of the image from Fig. 4A in which the Au nanoclusters can be distinguished; however, these are at the limit of our TEM's resolution. Interestingly, Au nanoclusters are not evenly distributed throughout the film, but rather there are regions with a high density of particles interspersed with areas with few to no particles. It is possible that smaller nanoclusters that are not resolved by our instrument are present in these polymer rich domains; however, this will be the focus of future work.

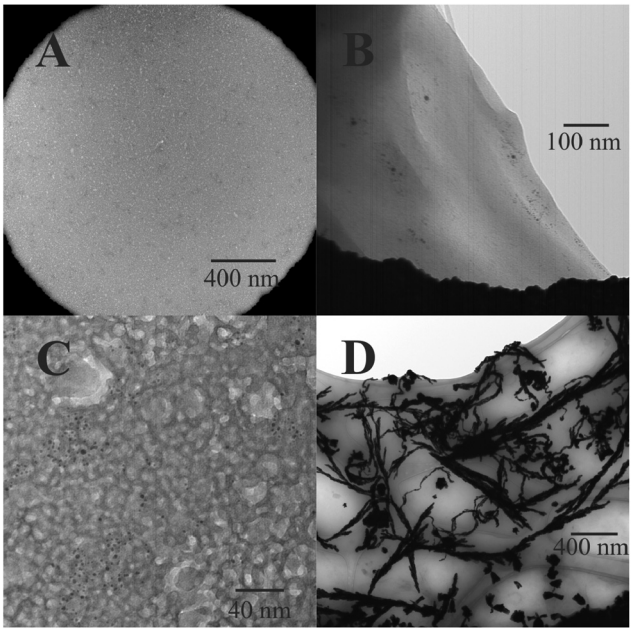

Fig. 4 TEM micrographs of nanocomposite material generated deposited on 2 μm diameter holey Au TEM grids using Cells 2 (left-hand side, (A) and (C) or Cell 1 (B), with [$KAuCl_4$] = 5 mM and c_m = 1 mM, after 25 CV scans at 0.020 V s^{-1}. (D) Nanocomposite material sampled onto a lacey-carbon 200 mesh Cu TEM grid after a ~5 min shake-flask experiment with 10 mM $KAuCl_4$(aq) combined with a DCE phase containing 10 mM of **1** and 10 mM of $P_{66614}TB$.

Moving forward, a shake-flask experiment was used in which a 10 mM solution of $KAuCl_4$ in 500 μL of aqueous phase was combined and mixed with 500 μL of DCE containing 10 mM of **1** and $P_{66614}TB$ in a 2 mL vial, *i.e.*, a large ITIES. Immediately after shaking, the yellow colour of the $KAuCl_4$ containing aqueous phase disappeared, and the organic phase turned from colourless to black. A 200 mesh Cu TEM grid was immersed and stirred in the solution, then dried and imaged. Fig. 4D shows the TEM micrograph obtained, in which long polymer strands with embedded Au NPs can be observed. Differentiating individual NPs was difficult and a proper size analysis was not possible; however, they appear to be in the range of 10–20 nm in diameter. These observations, combined with the intermediate hydrophobicity of $AuCl_4^-$/$AuCl_{(4-\gamma)}(OH)_\gamma^-$, suggest that the Au salt likely partitions into the DCE phase and undergoes homogeneous electron transfer to generate these Au NP coated polymer strands. This mechanism agrees with our recent work at the w|DCE micro interface in which a large negative current offset was observed in the presence of TT, indicating spontaneous $AuCl_4^-$/$AuCl_{(4-\gamma)}(OH)_\gamma^-$ transfer.[9] Even without mixing, Au NP/poly-bis(DTF)pyrene

strands formed in <5 min, suggesting that the bulk, homogeneous organic phase reaction at a large ITIES is rapid and spontaneous. However, these results indicate that by restricting the size of the ITIES and rapidly controlling the potential difference across the interface, one can restrict the reaction to a heterogeneous process and control nanocluster/polymer film formation.

TEM imaged nanoclusters were sized using ImageJ software with data compiled into histograms shown in Fig. 5A–F which were fit using a Gaussian function (red traces). The peak from the Gaussian fitting was taken to be the average nanocluster size and Fig. 5G depicts a plot of the average diameter with respect to c_m. As c_m increases, there is a concomitant decrease in nanocluster diameter. This is likely owing to an increase in the overall rate of the reaction which in turn likely means faster envelopment of the nanclusters in polymer matrix, limiting their final size.

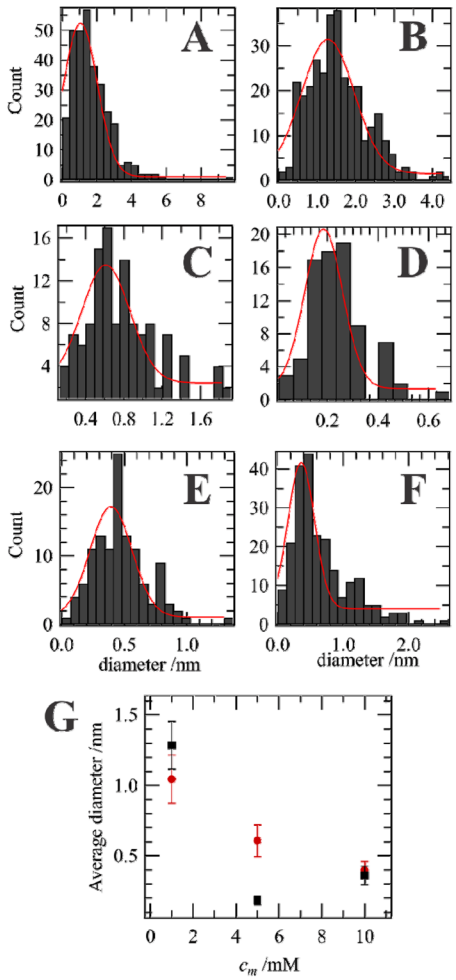

Fig. 5 Histograms of nanoparticle (NP) diameters obtained from TEM micrographs (see Fig. 4) using Cell 1 (left-hand side) and Cell 2 (right-hand side) while increasing c_m to 1 (A and B), 5 (C and D), and 10 mM (E and F); red curves are Gaussian fittings. (G) Trend in the average nanocluster diameter at pH 2 (●) and 5.5–6 (■) with increasing c_m; error bars are based on 3 standard deviations.

Next, Au nanocluster/poly-bis(DTF)pyrene films were similarly prepared and deposited onto glass substrates, then imaged using SEM. A low and high magnification SEM micrograph of the film obtained using Cell 1 with [$KAuCl_4$] = 5 mM, c_m = 10 mM, with an aqueous pH = 2, and after performing 25 CV cycles is shown in Fig. 6A and B, respectively. The spherical particles dispersed evenly across the films surface are larger Au NPs. Fig. 6C shows a histogram of the Au NP diameter with a median value of 50 nm. Since the droplet was ejected from the micropipette, the upward facing side of the Au NP/poly-bis(DTF)pyrene film would be towards the aqueous solution phase. These data are similar to our recent Au NP/poly-TT nanocomposite films;[9] whereby, the NP electrogeneration/electropolymerization process was proposed to occur in stages. Initially, the Au salt and monomer interact directly across the ITIES and the oxidized monomer can act as a capping agent. However, as the polymer film occludes the interface and the film thickness increases, the oxidized monomer no longer has access to the forming NPs. Nevertheless, the polymer is conductive and can mediate electron transfer between the organic and aqueous phases. Thus, Au NPs continue to be generated on the aqueous side; however, since diffusive access of the monomer/capping agent is likely limited by the growing film, these particles are larger on the aqueous side than on the organic one.

When deposited on the glass substrate the film was ~1 mm in diameter and circular. This is several orders of magnitude larger than the ITIES (25 μm in diameter). During electroge-

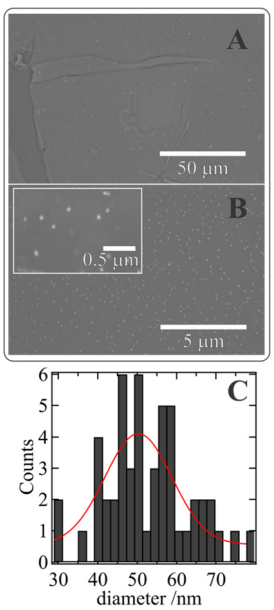

Fig. 6 (A) SEM image of nanocomposite thin film deposited on a glass slide. Film was electrosynthesized using 25 CV cycles at a micro-ITIES using Cell 1 with 5 mM $KAuCl_4$ (aq) and 10 mM **1** (DCE). (B) Magnified section from (A) with, inset, a further increase in the order of magnification. (C) Histogram of Au NP diameters measured from the images shown in panels A and B; red trace is the product of Gaussian curve fitting.

neration, the ITIES was monitored continuously using a CCD camera attached to a magnifying lens assembly and a black film was observed to grow into the aqueous side, up the microchannel. Based on these observations, it is likely that the film folds as it grows and has projections into the water side of the interface. This may be owing to the low solubility of the polymer in the aqueous phase and relatively higher solubility in the DCE phase.

Subsequently, films were deposited on conductive Au substrates and analyzed using atomic force microscopy (AFM) as well as in the Kelvin probe force microscopy configuration (KPFM) to measure the topography and surface potential/local work function of the films. In dual-pass, amplitude modulation KPFM mode, the electrostatic force (F_{es}) between the AFM tip and the substrate is related to the externally applied or direct voltage (V_{DC}) and the alternating voltage ($V_{AC}(\omega,t) = V_0 \sin(\omega t)$) by the following relation,[43–45]

$$F_{es}(z,t) = -\frac{1}{2}\frac{\partial C(z)}{\partial z}[(V_{CPD} \pm V_{DC}) + V_0 \sin(\omega t)]^2 \quad (4)$$

in which ω is the alternating voltage angular frequency, V_0 is the amplitude of the alternating voltage wavefunction, t is time, and $\partial C(z)/\partial z$ is the capacitance gradient between the tip and sample surface.[43–45] V_{CPD} is the contact potential difference as defined by,

$$V_{CPD} = \frac{\phi_{tip} - \phi_{sample}}{-e_0} \quad (5)$$

whereby, ϕ_{tip} and ϕ_{sample} are the work functions of the tip and sample, while e_0 is the elementary electronic charge (1.601×10^{-19} C). eqn (4) can be separated into 3 components,[43–45]

$$F_{DC} = -\frac{\partial C(z)}{\partial z}\left[\frac{1}{2}(V_{DC} \pm V_{CPD})^2\right] \quad (6)$$

$$F_{\omega} = -\frac{\partial C(z)}{\partial z}(V_{DC} \pm V_{CPD})V_0 \sin(\omega t) \quad (7)$$

$$F_{2\omega} = \frac{\partial C(z)}{\partial z}\frac{1}{4}V_0^2[\cos(2\omega t) - 1] \quad (8)$$

F_{ω} is the relationship employed to measure V_{CPD} in which V_{DC} and V_{AC} are controlled to nullify the effects of the mechanical AFM tip or electrical force oscillations, such that F_{ω} is a function of only V_{CPD} and V_{AC}; thus, the surface potential or work function values can be extracted.

Fig. 7 shows KPFM images for Au NP/poly-bis(DTF)pyrene films deposited on Au substrates with work functions varying between 5.03 to 5.34 eV. Average bulk, metallic Au has a work function of ~5.2 eV,[46] while most thiophene incorporated conductive polymer films, *e.g.*, PEDOT:PSS, are in the 4.8–5.6 eV range, which has been shown to be highly dependent on water content and polymer annealing.[47] Khoa *et al.*[48] recently showed a size dependence of Au NPs towards their work function; Au NPs deposited on graphene oxide demonstrated a decrease in work function from 5.73 to 5.35 eV when transitioning from 40 to 5 nm in size. Thus, the low work function

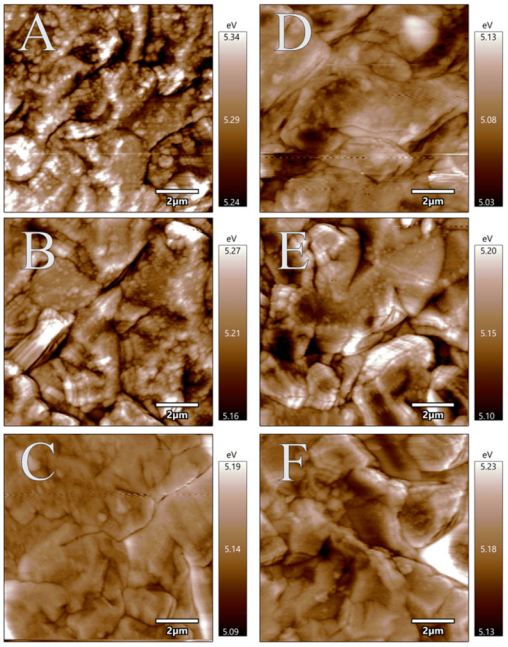

Fig. 7 Kelvin Probe Force Microscopy (KPFM) images obtained from films developed at a micro-ITIES after 25 CV scans and deposited on a gold substrate using Cells 1 (A–C) and 2 (D–F) with c_m = 1, 5, and 10 mM in DCE for the top, middle, and bottom rows, respectively. Scale bars are in eV.

regions within the KPFM images in Fig. 7, likely correspond to areas dense in Au nanoclusters.

AFM was used to measure the thickness of films deposited on glass slides. A roughly 1 μm × 1 μm area was excavated by the AFM tip to reveal the glass substrate and the area surrounding it scanned. Fig. 8B shows an example AFM image of a nanocomposite film electrogenerated at the micropipette interface after 25 CV scans and using Cell 2 with [$KAuCl_4$] = 5 mM and [1] 1 mM; whereby, the area labelled 'Well' corresponds to the section physically removed by the AFM tip. Fig. 8A shows a single line scan moving along the *x*-direction

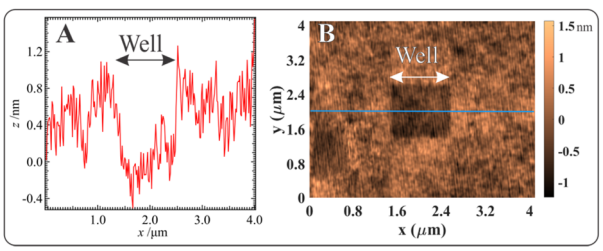

Fig. 8 (A) Cross-section of AFM topography obtain at a Au NP/poly-bis (DTF)pyrene film electrogenerated at a micro-ITIES after 25 CV cycles using Cell 2 with *x* and *y* equal to 5 and 1 mM and deposited on a glass substrate. (B) 2-Dimensional image of the film in which the blue line corresponds to the line trace from A. The area marked 'Well' was a section of the film excavated by the AFM tip to determine its thickness. The cross-section in A has been baseline corrected to the bottom of the 'Well' for emphasis.

and corresponding to the blue trace in Fig. 8B. Root-mean-square (RMS) analysis of the noise reveals a sensitivity of ±0.9 nm assuming three standard deviations, while the average distance from the top to the bottom of the Well was considered to be the film thickness. At moderate pH, films were well formed and averaged 3.0 nm thick. However, at pH 2 they were not and only two were successfully sampled. Using Cell 1 with [$KAuCl_4$] = 5 mM and [1] = 1 or 5 mM films were measured to be 139.4 and 1.6 nm, respectively. For the former, it is likely the film was folded in on itself complicating the analysis. The deposition of films onto other substrates, including metal and glassy-carbon electrodes, is ongoing, as well as their spread-ability/wet-ability on different materials; however, this is the focus of future work. Nevertheless, these results are compelling and indicate that extremely thin films with highly accessible nanoclusters are possible with this approach.

These results also point to two other phenomena. First, the large area and extremely thin characteristics of the final Au NP/poly-bis(DTF)pyrene film suggest that the film folds into the aqueous side owing to geometric confinement within the microchannel at the pipette tip. Visual observations made using the 12× zoom lens and CCD camera support this in that a dark area extending 25–50 μm up the microchannel was observed. Secondly, since the film is readily broken apart by ejection from the pipette, the inner glass walls of the microchannel likely act as nucleation sites with the nanocomposite film growing on the walls of the microchannel and along the ITIES, *i.e.*, the film is attached to the glass walls. Thus, this lowers the thermodynamic driving force needed to initiate Au NP generation/electropolymerization, hence the lower observed $\Delta_o^w\phi_{ET}$ *versus* the calculated value. Herein, we refer to this as the 'frozen pond' mechanism.

To measure the conductivity of the film, a Pt UME with a radius of 12.5 μm fixed above a 3-axis piezo-motor controlled stage, was brought into contact with Au coated slide with and without film deposited on the surface; Fig. 9A and B show the respective *i–V* curves recorded. The film was generated using Cell 2 with 5 mM of KCl and $KAuCl_4$ in the aqueous phase and 5 mM of **1** in DCE. The CV curve in Fig. 9A shows a typical response for a highly conductive material like Au with an ohmic response at roughly −0.9 V, *i.e.*, V = iR. Inverting the axes and using a linear fit of the current between the two plateau regions, one obtains a resistance of ~6 Ω. Next, the Au substrate coated with the Au nanocluster/poly-bis(DTF)pyrene composite shows a different *i–V* response which demonstrates negative resistance that resembles organic tunnel diodes as shown recently for organic semiconductors.[49–52] Nevertheless, performing the ohmic linear curve fitting one obtains a resistance of ~72 Ω. Based on this initial *i–V* profile, the film is likely an organic semiconductor; however, more work beyond the scope presented here needs to be done to characterize this property.

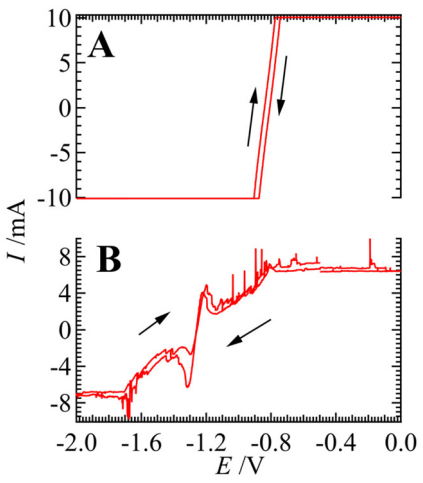

Fig. 9 *i–V* response curves for a 25 μm diameter Pt UME in contact with an unmodified Au coated silicon slide (A) and a slide modified with the Au nanocluster/poly-bis(DTF)pyrene film generated using Cell 2 (see Scheme 1) with 5 mM $KAuCl_4$(aq) and 5 mM **1** (DCE) (B).

Conclusions

Herein, simultaneous, electrochemically controlled Au nanocluster electrogeneration and polymerization of a dithiafulvenyl-substituted pyrene molecule at a micro liquid|liquid interface has been demonstrated. Miniaturization of the ITIES facilitates external electrolytic control of the nanocluster-embedded film that would otherwise proceed *via* a spontaneous homogeneous reaction in the bulk organic phase. Moreover, the combination of the specialized bis(DTF)pyrene molecule with the micro-ITIES platform permits electrodeless generation of extremely small (<1.7 nm) Au clusters. Altering the pH of the aqueous phase resulted in relatively poor film formation at low pH, while improved film at moderate pH, which agrees with thermodynamic calculations of $\Delta_o^w\phi_{ET}$.

Based on AFM and visual observations the film experiences nucleation at the glass surface along the inner walls of the micropipette and grows across the ITIES surface, similar to ice freezing on a pond. Additionally, the film likely continues to grow even after covering the ITIES, folding up and into the aqueous phase.

The as-prepared films offer a facile strategy for generating low dispersity Au nanocluster embedded conductive polymer films that can be used to modify a variety of substrates for surface enhanced Raman spectroscopy (SERS) or electrocatalysis, as well as a variety of other applications.

Author contributions

R. M.: Formal analysis, investigation, writing—review & editing, validation. K. R.: Formal analysis, investigation. E. P. C: Formal analysis, investigation. J. C. W.: Formal analysis, investigation. E. M.: Conceptualization, methodology, supervision, project administration, funding acquisition. G. J. B.: Conceptualization, methodology, writing – review & editing,

supervision, funding acquisition. T. J. S.: Conceptualization, methodology, writing—original draft, writing—review & editing, validation, supervision, project administration, funding acquisition. All authors have read and agreed to the published version of the manuscript.

Conflicts of interest

There are no conflicts to declare.

Acknowledgements

TJS would like to thank the Natural Sciences and Engineering Research Council (NSERC) for a Discovery Grant (#006074-2019) as well as Memorial University of Newfoundland for start-up funding. EM is grateful to the Canada Foundation for Innovation (CFI) for instrument funding, Memorial University's School of Graduate Studies and Vice President of Research for personnel funding.

References

1 A. F. Molina-Osorio, S. Yamamoto, I. Robayo-Molina, A. Gamero-Quijano, H. Nagatani and M. D. Scanlon, *Chem. Sci.*, 2021, **12**, 10227–10232.
2 A. F. Molina-Osorio, J. A. Manzanares, A. Gamero-Quijano and M. D. Scanlon, *J. Phys. Chem. C*, 2020, **124**, 18346–18355.
3 H. A. Al Nasser, C. Kim, Q. Li, M. A. Bissett, S. J. Haigh and R. A. W. Dryfe, *Electrochim. Acta*, 2022, **424**, 140609.
4 M. D. Scanlon, E. Smirnov, T. J. Stockmann and P. Peljo, *Chem. Rev.*, 2018, **118**, 3722–3751.
5 E. Smirnov, P. Peljo, M. D. Scanlon and H. H. Girault, *ACS Nano*, 2015, **9**, 6565–6575.
6 E. Smirnov, M. D. Scanlon, D. Momotenko, H. Vrubel, M. A. Méndez, P.-F. Brevet and H. H. Girault, *ACS Nano*, 2014, **8**, 9471–9481.
7 R. Moshrefi, A. Suryawanshi and T. J. Stockmann, *Electrochem. Commun.*, 2021, **122**, 106894.
8 R. A. Lehane, A. Gamero-Quijano, S. Malijauskaite, A. Holzinger, M. Conroy, F. Laffir, A. Kumar, U. Bangert, K. McGourty and M. D. Scanlon, *J. Am. Chem. Soc.*, 2022, **144**, 4853–4862.
9 R. Moshrefi, E. P. Connors, E. Merschrod and T. J. Stockmann, *Electrochim. Acta*, 2022, **426**, 140749.
10 A. Uehara, S. G. Booth, S. Y. Chang, S. L. M. Schroeder, T. Imai, T. Hashimoto, J. F. W. Mosselmans and R. A. W. Dryfe, *J. Am. Chem. Soc.*, 2015, **137**, 15135–15144.
11 U. Evans-Kennedy, J. Clohessy and V. J. Cunnane, *Macromolecules*, 2004, **37**, 3630–3634.
12 K. Gorgy, F. Fusalba, U. Evans, K. Kontturi and V. J. Cunnane, *Synth. Met.*, 2001, **125**, 365–373.
13 M. Vignali, R. Edwards and V. J. Cunnane, *J. Electroanal. Chem.*, 2006, **592**, 37–45.
14 M. Vignali, R. A. H. Edwards, M. Serantoni and V. J. Cunnane, *J. Electroanal. Chem.*, 2006, **591**, 59–68.
15 V. J. Cunnane and U. Evans, *Chem. Commun.*, 1998, 2163–2164, DOI: 10.1039/A806365F.
16 K. Maeda, H. Jänchenová, A. Lhotský, I. Stibor, J. Budka and V. r. Mareček, *J. Electroanal. Chem.*, 2001, **516**, 103–109.
17 C. Johans, P. Liljeroth and K. Kontturi, *Phys. Chem. Chem. Phys.*, 2002, **4**, 1067–1071.
18 C. Johans, K. Kontturi and D. J. Schiffrin, *J. Electroanal. Chem.*, 2002, **526**, 29–35.
19 C. Johans, J. Clohessy, S. Fantini, K. Kontturi and V. J. Cunnane, *Electrochem. Commun.*, 2002, **4**, 227–230.
20 C. Johans, R. Lahtinen, K. Kontturi and D. J. Schiffrin, *J. Electroanal. Chem.*, 2000, **488**, 99–109.
21 R. Knake, A. W. Fahmi, S. A. M. Tofail, J. Clohessy, M. Mihov and V. J. Cunnane, *Langmuir*, 2005, **21**, 1001–1008.
22 R. Moshrefi, H. Przybyła and T. J. Stockmann, *Sci. Rep.*, 2023, **13**, 1201.
23 U. Barsch and F. Beck, *Electrochim. Acta*, 1996, **41**, 1761–1771.
24 P. G. Ghasemabadi, T. Yao and G. J. Bodwell, *Chem. Soc. Rev.*, 2015, **44**, 6494–6518.
25 A. Mateo-Alonso, *Chem. Soc. Rev.*, 2014, **43**, 6311–6324.
26 T. M. Figueira-Duarte and K. Müllen, *Chem. Rev.*, 2011, **111**, 7260–7314.
27 M. Khadem and Y. Zhao, *J. Org. Chem.*, 2015, **80**, 7419–7429.
28 S. Liang, Y. Zhao and A. Adronov, *J. Am. Chem. Soc.*, 2014, **136**, 970–977.
29 H. Adows and Y. Zhao, *Chem. Commun.*, 2016, **52**, 13101–13104.
30 M. Khadem, J. C. Walsh, G. J. Bodwell and Y. Zhao, *Org. Lett.*, 2016, **18**, 2403–2406.
31 T. J. Stockmann and Z. Ding, *J. Phys. Chem. B*, 2012, **116**, 12826–12834.
32 T. J. Stockmann, A.-M. Montgomery and Z. Ding, *Can. J. Chem.*, 2012, **90**, 836–842.
33 M. Zhou, S. Gan, L. Zhong, X. Dong, J. Ulstrup, D. Han and L. Niu, *Phys. Chem. Chem. Phys.*, 2012, **14**, 3659–3668.
34 T. J. Stockmann, R. Guterman, P. J. Ragogna and Z. Ding, *Langmuir*, 2016, **32**, 12966–12974.
35 M. Luty-Błocho, K. Pacławski, M. Wojnicki and K. Fitzner, *Inorg. Chim. Acta*, 2013, **395**, 189–196.
36 M. Luty-Błocho, M. Wojnicki and K. Fitzner, *Int. J. Chem. Kinet.*, 2017, **49**, 789–797.
37 A. Uehara, S.-Y. Chang, S. G. Booth, S. L. M. Schroeder, J. F. W. Mosselmans and R. A. W. Dryfe, *Electrochim. Acta*, 2016, **190**, 997–1006.
38 S. Liu, Q. Li and Y. Shao, *Chem. Soc. Rev.*, 2011, **40**, 2236–2253.
39 P. Vanýsek, in *CRC Handbook of Chemistry and Physics*, ed. W. M. Haynes, CRC Press/Taylor, Boca Raton, FL, 2021, pp. 8.20–28.29.
40 S. Bai, C. Liu and L. Wang, *Langmuir*, 2021, **37**, 10741–10749.

41 R. Moshrefi and T. J. Stockmann, *Nanomaterials*, 2022, **12**, 2748.
42 M. A. Méndez, R. Partovi-Nia, I. Hatay, B. Su, P. Y. Ge, A. Olaya, N. Younan, M. Hojeij and H. H. Girault, *Phys. Chem. Chem. Phys.*, 2010, **12**, 15163–15171.
43 W. Melitz, J. Shen, A. C. Kummel and S. Lee, *Surf. Sci. Rep.*, 2011, **66**, 1–27.
44 V. Panchal, R. Pearce, R. Yakimova, A. Tzalenchuk and O. Kazakova, *Sci. Rep.*, 2013, **3**, 2597.
45 L. Liu and G. Li, *Appl. Phys. Lett.*, 2010, **96**, 083302.
46 *CRC Handbook of Chemistry and Physics*, ed. J. R. Rumble, CRC Press/Taylor & Francis, Boca Raton, FL, 2022.
47 N. Koch, A. Vollmer and A. Elschner, *Appl. Phys. Lett.*, 2007, **90**, 043512.
48 N. T. Khoa, S. W. Kim, D.-H. Yoo, E. J. Kim and S. H. Hahn, *Appl. Catal., A*, 2014, **469**, 159–164.
49 S. Ragul, R. Dhar, S. Dutta and D. Ray, *Org. Electron.*, 2022, **101**, 106399.
50 S. Conti, C. Martínez-Domingo, M. Lay, L. Terés, F. Vilaseca and E. Ramon, *Adv. Mater. Technol.*, 2020, **5**, 1900773.
51 M. Cao, W. J. Hyun, L. F. Francis and C. D. Frisbie, *Flexible Printed Electron.*, 2020, **5**, 015006.
52 F. A. Viola, B. Brigante, P. Colpani, G. Dell'Erba, V. Mattoli, D. Natali and M. Caironi, *Adv. Mater.*, 2020, **32**, 2002329.